

DESIGN OF A PARAXIAL INVERSE COMPTON SCATTERING DIAGNOSTIC FOR AN INTENSE RELATIVISTIC ELECTRON BEAM

J.E. Coleman[†], J.A. Oertel, C.A. Ekdahl, D. Shaw, T.N. Archuleta, D.C. Moir, B.T. McCuistian, and M.T. Crawford

Los Alamos National Laboratory, Los Alamos, NM, United States

Y. Platonov

Rigaku Innovative Technologies, Inc., Auburn Hills, MI, United States

Abstract

An inverse Compton scattering diagnostic is currently being developed for an 80 ns, intense relativistic electron bunch with an energy of 19.8 MeV and nominal current of 1.7 kA. The principal purpose of this diagnostic is to provide a measurement of the 6-D phase space distribution of the electron beam in a single shot without disrupting its axial propagation. The electron beam is intercepted by 450 mJ of green light, which is upscattered into the soft X-ray range by the relativistic electrons. The diverging, scattered photons are diffracted onto an X-ray framing camera by an X-ray crystal concentric to the beam pipe utilizing an elongated von Hamos geometry [1]. The experimental configuration is presented, which includes the electron and photon interaction dynamics, crystal design, X-ray framing camera design, and the expected time resolved longitudinal and transverse distributions.

I. INTRODUCTION

Non-invasive optical scattering techniques began development 90 years ago [2] and have been utilized as light sources or diagnostic techniques for over 40 years. Thomson scattering has been used to measure n_e and T_e for low temperature and high temperature plasmas with $n_e < 10^{21} \text{ m}^{-3}$ [3]. In addition it has been used to measure n_e , T_e , and T_i in solid density plasmas ($n_e > 10^{28} \text{ m}^{-3}$) [4-8].

Inverse Compton measurements have been made on accelerators with energy ranges from 22-60 MeV, beam currents of 0.14-140 A, or $3 \times 10^9 - 10^{10}$ electrons/bunch. [9-11]. These results have sparked interest to use these methods as non-invasive beam diagnostics or laser wire scanners, in addition to X-ray and gamma light sources. These methods are even proposed for the development of a compact EUV source by scattering a high power CO₂ laser light off a 7 MeV e⁻ beam [12].

The Dual-Axis Radiography for Hydrodynamic Testing (DARHT) facility has been interested in developing non-invasive beam diagnostics since the facility began experiments in 1990 [13]. The function of the facility and intensity of the beams on Axes 1 and 2, limit beam studies with intercepting diagnostics. DARHT is exploring the capability of a paraxial grazing incidence spectrometer to provide a measurement of the 6-D phase space. This design for DARHT Axis-1 is unique because the beam

has $\sim 10^{14}$ electrons/bunch, several orders more than refs [9-11], and we plan to perform these measurements without bending the electron beam 90° out of the detection plane.

The technique being proposed here utilizes both the fundamentals of Compton upscatter in the accelerator community and X-ray diffraction methods used in the Inertial Fusion community. X-ray Thomson scattering methods utilizing Bragg crystals is routinely used for X-ray imaging in relatively the same energy range [6-8,14-17]. However they use X-ray laser probes to interrogate solid density plasmas and measure the Compton downshift.

II. EXPERIMENTAL SETUP

The experimental configuration used to deploy the inverse Compton diagnostic is the downstream transport section of DARHT Axis-1 (Fig. 1). The 60 ns, 19.8 MeV electron bunch, with a nominal current of 1.7 kA, is intercepted by a 10 ns, 450 mJ, frequency doubled (532 nm) pulsed Nd:YAG laser [18] at Box 9 ($z = 34.5 \text{ m}$). The visible green light is upscattered into the soft X-ray range and diverges from the interception point downstream at an angle $\theta_s = 1/\gamma \sim 25 \text{ mrad}$. Ignoring thermal spread in the beam due to emittance, the most upstream detection plane of the scattered radiation, where the radiation grazes the beam pipe, is nearly 3 m downstream of the interaction point. However, detection at this plane only gives the experimenter information about the transverse distribution of the beam and not the energy. In order to detect and resolve the energy of the upscattered soft X-rays a calibrated detector or a spectrometer must be used. In our case because of the path lengths of interest we have chosen to use X-ray Bragg crystals, which act like a grating in a visible spectrometer, to diffract the X-ray photons to our detector plane. Since the path length from the interception point and the detection point is slightly over 3.7 m and the radiation forward scatters at 25 mrad, it is logical to place the Bragg crystal outside of the path of the beam half way between the scattering and detection point. In addition, this optimizes mosaic focusing with a curved Bragg crystal, 1:1 optics, and no magnification.

[†] This work was supported by the National Nuclear Security Administration of the U.S. Department of Energy under

[‡] email: jecoleman@lanl.gov

Report Documentation Page				Form Approved OMB No. 0704-0188	
Public reporting burden for the collection of information is estimated to average 1 hour per response, including the time for reviewing instructions, searching existing data sources, gathering and maintaining the data needed, and completing and reviewing the collection of information. Send comments regarding this burden estimate or any other aspect of this collection of information, including suggestions for reducing this burden, to Washington Headquarters Services, Directorate for Information Operations and Reports, 1215 Jefferson Davis Highway, Suite 1204, Arlington VA 22202-4302. Respondents should be aware that notwithstanding any other provision of law, no person shall be subject to a penalty for failing to comply with a collection of information if it does not display a currently valid OMB control number.					
1. REPORT DATE JUN 2013		2. REPORT TYPE N/A		3. DATES COVERED -	
4. TITLE AND SUBTITLE Design Of A Paraxial Inverse Compton Scattering Diagnostic For An Intense Relativistic Electron Beam				5a. CONTRACT NUMBER	
				5b. GRANT NUMBER	
				5c. PROGRAM ELEMENT NUMBER	
6. AUTHOR(S)				5d. PROJECT NUMBER	
				5e. TASK NUMBER	
				5f. WORK UNIT NUMBER	
7. PERFORMING ORGANIZATION NAME(S) AND ADDRESS(ES) Los Alamos National Laboratory, Los Alamos, NM, United States				8. PERFORMING ORGANIZATION REPORT NUMBER	
9. SPONSORING/MONITORING AGENCY NAME(S) AND ADDRESS(ES)				10. SPONSOR/MONITOR'S ACRONYM(S)	
				11. SPONSOR/MONITOR'S REPORT NUMBER(S)	
12. DISTRIBUTION/AVAILABILITY STATEMENT Approved for public release, distribution unlimited					
13. SUPPLEMENTARY NOTES See also ADM002371. 2013 IEEE Pulsed Power Conference, Digest of Technical Papers 1976-2013, and Abstracts of the 2013 IEEE International Conference on Plasma Science. IEEE International Pulsed Power Conference (19th). Held in San Francisco, CA on 16-21 June 2013., The original document contains color images.					
14. ABSTRACT An inverse Compton scattering diagnostic is currently being developed for an 80 ns, intense relativistic electron bunch with an energy of 19.8 MeV and nominal current of 1.7 kA. The principal purpose of this diagnostic is to provide a measurement of the 6-D phase space distribution of the electron beam in a single shot without disrupting its axial propagation. The electron beam is intercepted by 450 mJ of green light, which is upscattered into the soft X-ray range by the relativistic electrons. The diverging, scattered photons are diffracted onto an X-ray framing camera by an X-ray crystal concentric to the beam pipe utilizing an elongated von Hamos geometry [1]. The experimental configuration is presented, which includes the electron and photon interaction dynamics, crystal design, X-ray framing camera design, and the expected time resolved longitudinal and transverse distributions.					
15. SUBJECT TERMS					
16. SECURITY CLASSIFICATION OF:			17. LIMITATION OF ABSTRACT SAR	18. NUMBER OF PAGES 6	19a. NAME OF RESPONSIBLE PERSON
a. REPORT unclassified	b. ABSTRACT unclassified	c. THIS PAGE unclassified			

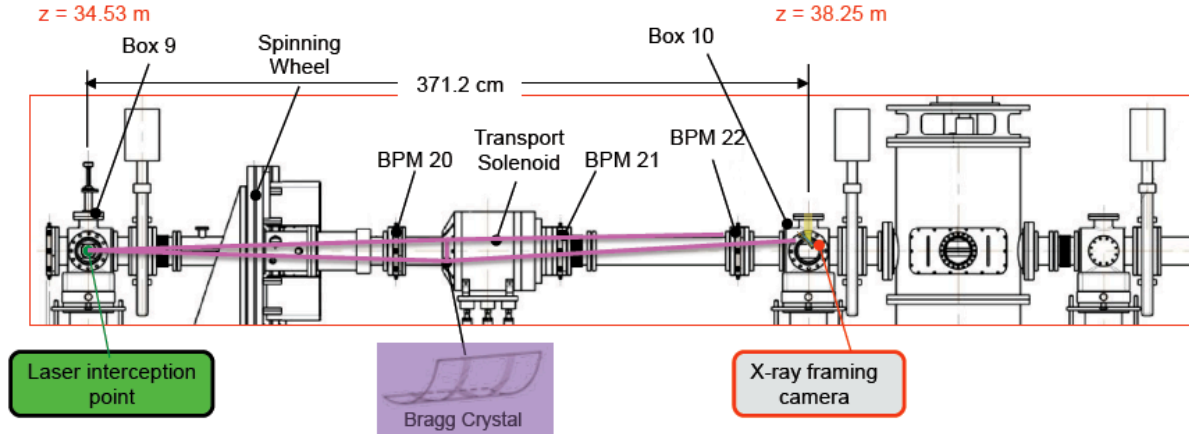


Figure 1. Elevation view of the DARHT Axis-1 downstream configuration used to intercept the electron beam and diagnose its longitudinal and transverse distribution. The z-locations indicate their axial distance relative to the cathode face ($z = 0$).

III. SCATTERING PHYSICS

Compton scattering is the inelastic scattering of electromagnetic radiation by a free charged particle, such as an electron. In the Thomson limit the energy of the incident photons $E_i \ll m_e c^2$. However, in our case the electron beam $E_{\text{beam}} \gg m_e c^2 \gg E_i$ so the incident photon radiation is upscattered by the relativistic electrons.

The relationship of the scattered photons to the incident photons can be derived through trigonometry as has been done by refs [11,19].

$$E_s = E_i \frac{1 + \beta \cos \theta_i}{1 - \beta \cos \theta_s}, \quad (1)$$

Setting $\theta_i = \theta_s = 0$ for a parallel electron-photon collision, $\beta \sim 1 - 1/\gamma^2$ for $\gamma \gg 1$, the scattered photons have a maximum forward energy of:

$$E_s = 2\gamma^2 E_i, \quad (2)$$

where E_s is the scattered photon energy, γ is the Lorentz factor, and E_i is the incident photon energy. The scattered energy spectrum as a function of incident angle for the Axis-1 (19.8 MeV) and Axis-2 (16.5 MeV) [20] beams intercepted by the fundamental (1064 nm) and frequency doubled (532 nm) Nd:YAG wavelengths are shown in Fig. 2. In the beam frame electron beams with $\gamma \gg 1$, as is the case here, only see the incident photon radiation at $\theta_i \sim 1/\gamma$, so the photons are always forward scattered at $\theta_s \sim 1/\gamma$.

The number of photons yielded is a function of the target, scattering source, and the cross section of their reaction:

$$N_\gamma = \frac{n_e L \sigma_c \lambda E_l}{hc}, \quad (3)$$

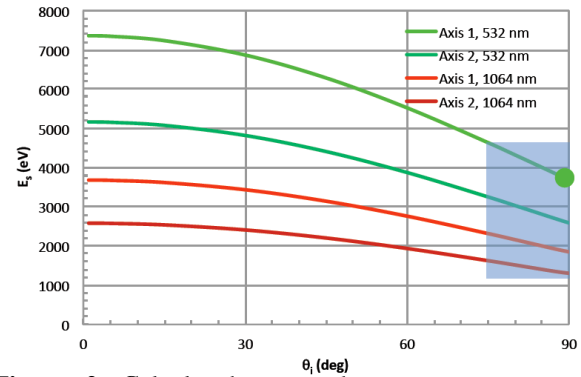


Figure 2. Calculated scattered energy spectrum as a function of incident angle for the Axis 1 and 2 beams with the fundamental (1064 nm, red) and frequency doubled (532 nm, green) Nd:YAG wavelengths. The shaded region on the right of the curve indicates the experimental parameter space. The green dot indicates the actual scattered energy we plan to produce.

In this case the electron density, n_e , and the interaction length, L , is the target, the incident number of photons is $\lambda E_l / hc$, and the Compton cross-section for these beam energies is simply the Thomson cross section ($8\pi/3 r_e^2$). A more complex derivation of the Klein-Nishina differential cross section is used for beams with $\gamma > 10^4$, to estimate the Compton cross section as a function of scattering wavelength [19, 21-23]. The nominal tune for our 1.7 kA beam on Axis 1 has a 7.5 mm radius (Fig. 3). With a 450 mJ frequency doubled Spectra-Physics Quata-Ray Lab 170-10 Nd:YAG laser our number of incident photons should be just above 10^{18} [18]. The maximum photon yield for a Thomson scattering diagnostic is typically ~ 13 orders $<$ photon source due to the cross section of the reaction and we calculate 2×10^5 . Although this is a fairly respectable photon count, the amount of photons collected by the detector will be much less due to expansion losses of the scattered distribution from emittance (Fig. 3) and the solid angle of photons either directly detected or diffracted by the crystal. These details will be discussed further below in Section IV.D.

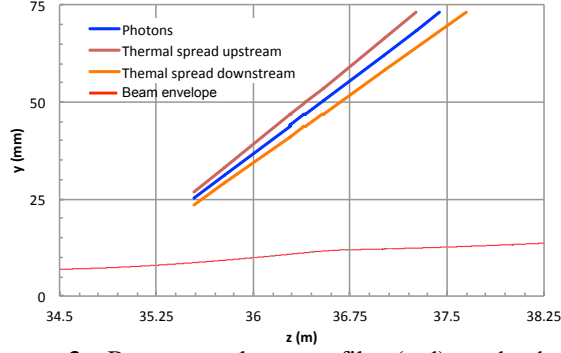


Figure 3. Beam envelope profile (red) and photon expansion along the beam axis (blue). The thermal spread upstream (maroon) and downstream (orange) is also plotted for the Axis-1 electron beam which has a thermal width of ~ 3 mrad.

IV. ICS SYSTEM DESIGN

As mentioned above we plan to deploy the diagnostic on the downstream transport section of DARHT Axis 1. The inverse Compton scattering (ICS) diagnostic consists of several components, shown in Figs. 1 & 4, these consist of the laser and its optics, a X-ray Bragg crystal, and the detector: an X-ray framing camera.

A. Laser optics

The laser optics consist of a 450 mJ, 532 nm, Spectra-Physics Quanta-Ray Lab 170-10 Nd:YAG laser [18] oriented parallel to the propagation axis of the beam. The laser beam is then bent horizontally 90° , with a 532 nm coated mirror and then focused to a ~ 1 mm spot, at the interception of the electron beam, with a 50 cm focal length plano-convex lens (Fig. 4). Prior to entering the vacuum the laser light passes through a Brewster angled window, which is used to compensate for the change in the index of refraction at the glass/vacuum interface and minimize scattering. After the laser exits the vacuum system it is terminated into a beam dump [24]. An insertable power meter is also installed to verify the beam energy per pulse is maintained for ICS [25].

Three additional configurations are under development and will be tested following the proof-of-principle experiments. These include using cylindrical optics to intercept the electron beam with a laser “sheet” to produce a higher photon yield and larger scattered distribution. The second involves using an array of mirrors for multiple laser passes to provide a series of scattered photon ribbons. Finally, either a longer laser pulse or high frequency laser pulse will be used for scattering measurements over the $1.6 \mu\text{s}$ pulse length of the Axis 2 electron beam [20].

B. Bragg crystal, diffraction crystal

The next key component in our ICS spectrometer design is the X-ray Bragg crystal used to diffract the expanding scattered soft X-rays to the detection plane. This technique is routinely used in the ICF community for X-ray imaging in relatively the same energy range [26-29]. After the scattered photons are produced at $z =$

34.5 m they begin to propagate forward in a cone with a half angle of $\theta_s = 1/\gamma \sim 25$ mrad.

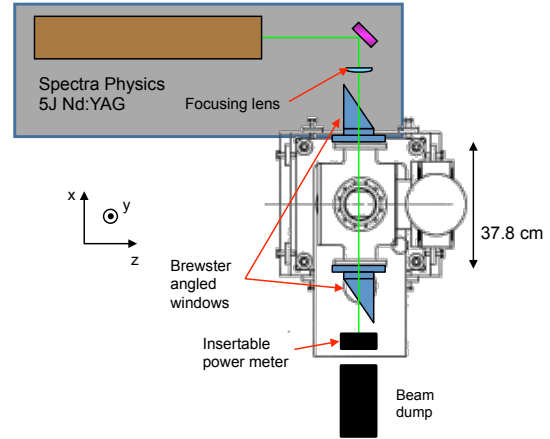


Figure 4. Laser configuration (top view) for interception at the exit of the accelerator, Box 9 ($z = 34.5$ m) on DARHT Axis 1 (not to scale).

When designing the crystal configuration relative to the scattering location and the detection location we designed an elongated von Hamos geometry [1] (Fig. 5). We wanted to utilize as much of the existing beamline as possible. In doing so we use Boxes 9 & 10 (Fig. 1) for our object and image planes. The top vertical vacuum port is the location of our detector, so it is logical to place the crystal on the bottom of the beam pipe. Establishing a line of sight between the object and image planes and a direct perpendicular line down to the crystal we set the constraints for our von Hamos geometry. We now have our radius of curvature, R_c for a curved crystal and the Bragg angle, θ_B , which is the angle between the rays and the diffraction plane (Fig. 5). To minimize magnification and to optimize mosaic focusing the ideal von Hamos geometry has focal distances $z_1 = z_2$. θ_s , shown in Fig. 5, sets the axial location of the crystal, z_o . Since it is only ~ 25 mrad $z_o \sim z_1 = 1.86$ m. At this location the scattered radiation cone has expanded to a radius of 47 mm which is a safe radial distance outside of the beam envelope (Fig. 3) to place the crystal.

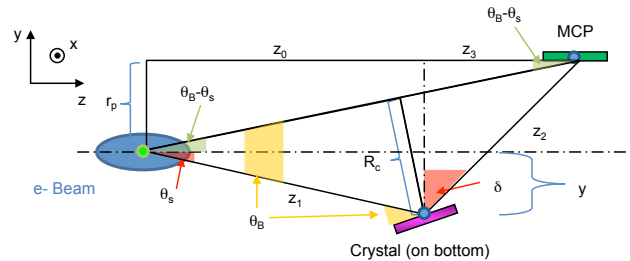


Figure 5. von Hamos spectrometer configuration for DARHT Axis 1 (not to scale).

The Bragg angle can be determined simply through trigonometry:

$$\sin \theta_B = \frac{R_C}{z_1}. \quad (4)$$

However, for our design we do not know the radius of curvature, so we must determine the Bragg angle utilizing Fig. 5:

$$\tan(\theta_B - \theta_s) = \frac{r_p}{z_o + z_3} = \frac{r_p}{\Delta z}, \quad (5)$$

where r_p is the pipe radius and Δz is the axial distance between the object and image planes (Boxes 9 & 10). The scattering angle and geometry we have constrains us to $\theta_B < 4^\circ$ (Fig. 6) and reduces the achievable energy resolution. Fig. 6 sets the design parameter space for multiple electron beams utilizing this method of ICS. It illustrates that the path length of the geometry for lower energy beams is shorter because it is proportional to the scattering angle. In addition the Bragg angles will be larger at lower energies. The design point for DARHT Axis-1 with a $\Delta z = 3.71$ m or $z_o = 1.86$ m sets our $\theta_B = 2.57^\circ$.

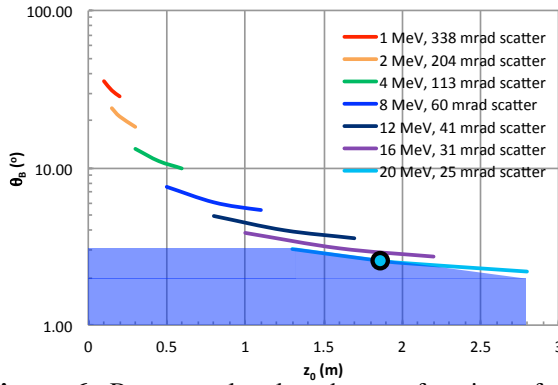


Figure 6. Bragg angle plotted as a function of axial distance from scattering location to crystal (z_o) and electron beam energy. The turquoise line applies to DARHT Axis-1 and the design point is circled. The purple line applies to DARHT Axis-2.

The constraint of a shallow Bragg angle limits our choices to large lattice spacing crystals as illustrated by Bragg's law:

$$n\lambda = 2d \sin \theta_B, \quad (6)$$

where n is the reflection order, λ is the wavelength of the scattered radiation, and d is the lattice spacing of the crystal. Returning briefly to the scattering physics in Section III, the scattered X-ray energy should be 3.68 keV for 532 nm laser light incident at 90° on a 19.8 MeV electron beam. The corresponding wavelength at this energy is 3.37 Å. The Bragg angles required for materials with different 2d lattice spacing (Table 1) are shown in Fig. 7. It is apparent from Fig. 7 that crystals with lattice spacings > 25 Å require too large of a Bragg angle for our application.

A multilayer optic was chosen because of its preferable optical properties; high-energy resolution, high reflectivity, and the lattice spacing and Bragg angle can be custom designed per customer application. After

setting the constraints for the crystal we partnered with Rigaku Innovative Technologies to design our multilayer optic. The crystal we initially designed is a flat crystal for a simple proof-of-principle experiment, however we plan to use a curved Bragg crystal to optimize the von Hamos geometry for the final design. The performance characteristics of the flat Cr/C crystal with a 2d lattice spacing of 8.46 nm are shown in Fig. 8. The energy resolution is limited to $\sim 5\%$ and the reflectivity is $> 30\%$. The performance of each of these parameters can be improved by $\sim 2\times$ by increasing the scattered photon energy, or reducing the lattice spacing, by 15%.

Table 1. Single layer X-ray crystal materials, their lattice spacing, and minimum energy range. Those highlighted in blue are the smallest lattice spacing applicable.

Type	2d (Angstroms)	Min Energy (eV)
LIF	4.028	3078.07
HOPG	6.708	1848.31
PET	8.742	1418.27
ADP	10.648	1164.39
TAP	25.75	481.49
RAP	26.1	475.04
KAP	26.6	466.11
ODPB	100	123.98

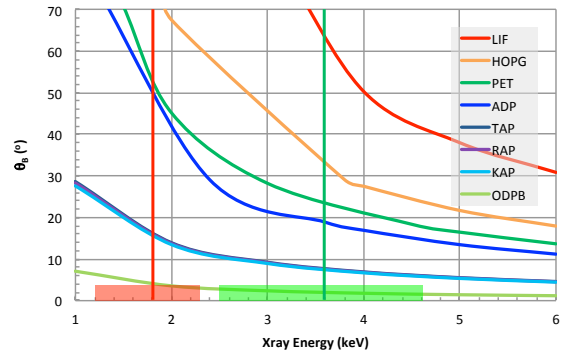


Figure 7. Bragg angle plotted as a function crystal materials and X-ray energy. The region highlighted in red is the relevant X-ray energy range for 1064 nm light upscattered by both DARHT Axes 1 & 2. The region highlighted in green is the relevant X-ray energy range for 532 nm light upscattered by both DARHT Axes 1 & 2.

C. X-ray framing camera

The final component to the ICS system is the detector. X-ray imaging techniques have been well developed in the ICF community [14-17]. The development of our X-ray framing camera is nearly identical to a design developed by ref. [14]. We are using a single strip micro-channel plate (MCP). The MCP is a Au coated SiO_2 wafer with 10 μm holes. The photocathode of the MCP is coated with Au because its quantum efficiency peaks near 3 keV in soft X-energy at 10-25%, depending on incident angle [30,31]. The MCP is mounted in a hermetically sealed housing and is electrically floating for pulsed gating capabilities. The pulse length and amplitude is addressable up to 4 kV and down to 40 ps to optimize the X-ray imaging efficiency. Our experiment we will only require 10 ns gates.

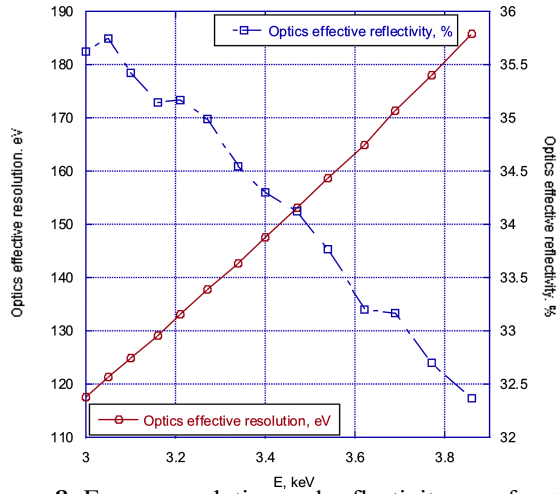


Figure 8. Energy resolution and reflectivity as a function of X-ray energy for Cr/C multilayer optic designed by Rigaku Innovative Technologies.

The MCP assembly is mounted at 45° with the top edge of the MCP flush with the beam pipe. A 25- μ m thick Al plate is used to attenuate any visible light or photons with energies < 1 keV from hitting the MCP [32]. After the soft X-ray photons incident on the MCP are converted to electrons, the electrons are then multiplied down the bore of the MCP. The electrons are then accelerated across a 50 μ m gap to a P43 phosphor that is coated onto a fiber optic face plate (FOFP) [33,34]. Once the electrons strike the phosphor it fluoresces and produces visible \sim 530 nm photons that are imaged by our CCD camera. The FOFP is 4 cm in diameter and composed of 6 μ m fibers arranged in a hexagonally close packed configuration to preserve maximum light transfer from the phosphor to the CCD. The CCD we use for imaging is a 1000 series large format CCD manufactured by Spectral Instruments [35].

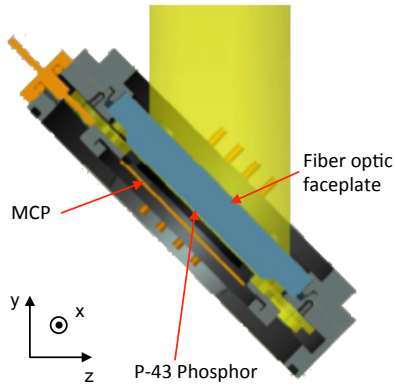


Figure 9. Layout of the X-ray framing camera used for the ICS system. Individual component are listed, the coordinate system is listed where the electron beam propagation axis is the z-axis and the y-axis is vertical.

D. Collection efficiency

The collection efficiency of our ICS system can be quantified as follows. The number of photons collected N_{γ_c} is calculated below:

$$N_{\gamma_c} = N_{\gamma_s} * \Omega * R * M * QE_{MCP} * CE_{Phos} * QE_{CCD}, (7)$$

where N_{γ_s} is the number of photons scattered, Ω is the solid angle, R is the reflectivity of the crystal, M is the multiplication factor of the MCP, QE_{MCP} is the quantum efficiency of photocathode for 3.68 keV soft X-ray photons to electrons, CE_{Phos} is the conversion efficiency of the photo-electrons to back to visible photons, and QE_{CCD} is the quantum efficiency of the CCD. Each of these values are either provided by the supplier or have been measured and documented in the references listed and are shown in Table 2. It is apparent that the MCP has nearly single photon counting capability. However, one of the biggest challenges to the detection capability of this system will be the background Bremsstrahlung X-rays generated in the accelerator.

Table 2. Tabulation of the contributing factors to the light collection efficiency of the ICS system.

N_{γ_c}	1.70E+08
N_{γ_s}	2.27E+05
Ω	0.01
R	0.3
$N_{\gamma_{MCP}}$	681.1
M	1.00E+04
QE_{MCP}	0.25
CE_{Phos}	200
QE_{CCD}	0.5

V. SCATTERED LIGHT DISTRIBUTIONS

The scattered light distributions we expect to measure at the detection plane with the X-ray framing camera are shown below in Fig. 10. In the first case (Fig. 10(a)), as discussed in Section IV.A., we plan to intercept the electron beam with a single 1-mm diameter laser pass. This should yield a single ribbon expanding downstream in which a small fraction of the photons will be diffracted by the crystal and detected by the X-ray framing camera. The next case (Fig. 10(b)) a laser sheet 15 mm wide will intercept the full electron beam distribution. This will yield a larger scattered photon distribution, which will require the curved Bragg crystal to focus and diffract the photons to the MCP. In both cases the measured distribution should yield details about both the transverse and longitudinal distributions of the beam, including the emittance and energy spread.

VI. CONCLUSIONS

We have developed a design for a paraxial inverse Compton scattering diagnostic. Utilizing a Bragg crystal, we are able to avoid bending the beam and use the available axial transport section of the accelerator to diagnose the beam.

We are using well-developed technologies for detection and plan to have quantitative results for our proof-of-principle experiment in the literature in the near future. In addition we have several iterations where improvements can be made for both the intercepting probe and the detection optics.

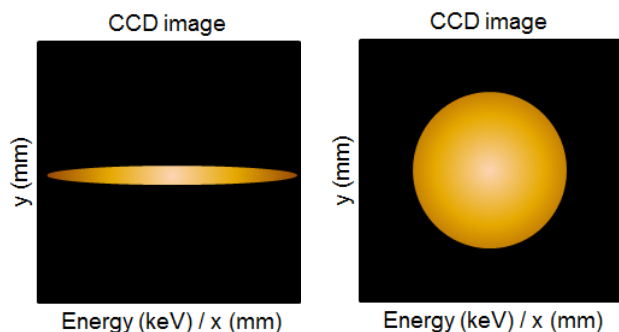


Figure 10. Expected scattered light distributions for (a) the proof-of-principle experiment with a single 1 mm diameter laser interception; and (b) an expanded laser sheet intercepting the full electron beam distribution.

VII. REFERENCES

- [1] L. v. Hamos, "Röntgenspektroskopie und Abbildung mittels gekrümmter Kristallreflektoren," *Naturwiss.*, vol. 20, pp. 705, (1932).
- [2] A. H. Compton, "A Quantum Theory of the Scattering of X-Rays by Light Elements," *Phys. Rev.* **21**, 483 (1923).
- [3] J. Sheffield, "The incoherent scattering of radiation from a high temperature plasma," *Plasma Phys.*, vol. 14, pp. 783 (1972).
- [4] S.H. Glenzer, "Demonstration of Spectrally Resolved X-Ray Scattering in Dense Plasmas," *Phys. Rev. Lett.*, vol. 90, no 17, pp. 175002 (2003).
- [5] D.H. Froula, "Thomson-scattering techniques to diagnose local electron and ion temperatures, density, and plasma wave amplitudes in laser produced plasmas," *Rev. Sci. Instrum.*, vol. 77, pp. 10E522 (2006).
- [6] S.H. Glenzer, "Observations of Plasmons in Warm Dense Matter," *Phys. Rev. Lett.*, vol. 98, pp. 065002 (2007).
- [7] A.L. Kritcher, "Measurements of Ionic Structure in Shock Compressed Lithium Hydride from Ultrafast X-ray Thomson Scattering," *Phys. Rev. Lett.*, vol. 103, pp. 245004 (2009).
- [8] A.L. Kritcher, "Ultrafast K α x-ray Thomson scattering from shock compresses lithium hydride," *Phys. Plasmas*, vol. 16, pp. 056308 (2009).
- [9] W. P. Leemans et al., "X-Ray Based Subpicosecond Electron Bunch Characterization Using 90 \pm Thomson Scattering," *Phys. Rev. Lett.*, vol. 77, pp. 4182, (1996).
- [10] I. V. Pogorelsky, "Demonstration of 8 x 10¹⁸ photons/second peaked at 1.8 Å in a relativistic Thomson scattering experiment," *Phys. Rev. ST Accel. Beams*, vol. 3, pp. 090702, (2000).
- [11] K. Chouffani, "Determination of electron beam parameters by means of laser-Compton scattering," *Phys. Rev. ST Accel. Beams*, vol. 9, pp. 050701, (2006).
- [12] S. Kashiwagi, "Compact EUV source based on laser Compton scattering between micro-bunch electron beam and CO₂ laser pulse," *Proceedings of EPAC08*, Genoa Italy, 2008.
- [13] T.P. Hughes, "High-brightness electron beam generation and transport," *J. Appl. Phys.*, vol. 68, no. 6, pp. 2562 (1990).
- [14] J.A. Oertel, "Dual microchannel plate module for a gated monochromatic x-ray imager," *Rev. Sci. Instrum.*, vol. 68, pp. 789 (1997).
- [15] J.A. Oertel, "The large format x-ray imager," *Rev. Sci. Instrum.*, vol. 72, pp. 701 (2001).
- [16] O.L. Landen, "Angular sensitivity of gated microchannel plate framing cameras," *Rev. Sci. Instrum.*, vol. 72, pp. 709 (2001).
- [17] M.B. Schneider, "Time-resolved soft x-ray imaging diagnostic for use at the NIF and OMEGA lasers," *Rev. Sci. Instrum.*, vol. 77, pp. 10E321 (2006).
- [18] http://www.newport.com/Quanta-Ray-Lab-Series-Pulsed-Nd-YAG-Lasers/368171/1033/info.aspx#tab_Specifications
- [19] C. Ekdahl, "Laser-light scattering diagnostics for ATA Propagation Experiments," AMRC-R-263, Mission Research Corporation, (1980).
- [20] C. Ekdahl, "Suppressing beam-centroid motion in a long-pulse linear induction accelerator," *Phys. Rev. ST Accel. Beams*, vol. 14, pp. 120401, (2011).
- [21] O. Klein, Y. Nishina, "Über die Streuung von Strahlung durch freie Elektronen nach der neuen relativistischen Quantendynamik von Dirac". *Z. Phys.*, vol. 52 (11-12), pp. 853 (1929).
- [22] P. Tenenbaum, "Measurement of small electron-beam spots," *Annu. Rev. Nucl. Part. Sci.*, vol. 49, pp. 125 (1999).
- [23] I. Agapov, "Beam emittance measurement with laser wire scanners in the International Linear Collider beam delivery system," *Phys. Rev. ST Accel. Beams*, vol. 10, pp. 112801, (2007).
- [24] <http://www.thorlabs.us/thorProduct.cfm?partNumber=BT610>
- [25] <http://www.ophiropt.com/laser-measurement-instruments/laser-power-energy-meters/products/power-sensors/thermal-high-power>
- [26] B. Yaakobi, "Crystal Diffraction Systems for X-ray Spectroscopy, Imaging, and Interferometry of Laser Fusion Targets," *IEEE J. Quantum Electron.*, vol. QE-19, no. 12, pp. 1841 (1983).
- [27] F.J. Marshall, "A framed monochromatic x-ray microscope for ICF," *Rev. Sci. Instrum.*, vol. 68, pp. 735 (1997).
- [28] A.P. Shevelko, "Compact focusing von Hamos spectrometer for quantitative x-ray spectroscopy," *Rev. Sci. Instrum.*, vol. 73, pp. 3458, (2002).
- [29] H. Legall, "Applications of Highly Oriented Pyrolytic Graphite (HOPG) for x-ray diagnostics and spectroscopy," *Proc. of SPEI*, vol. 5918, pp. 11 (2005).
- [30] T. Cho, "Quantum efficiency of gold photocathodes (2–8 keV) and EXAFS in its secondary electron yield and in the detection currents of a microchannel plate and a silicon surface barrier detector," *Rev. Sci. Instrum.*, vol. 59, pp. 2453 (1988).
- [31] G.W. Fraser, "The characterisation of gold X-ray photocathodes," *Nucl. Instr. Meth. A*, vol. 321, pp. 385 (1992).
- [32] A.L. Kritcher, "Ultrafast K- α Thomson Scattering from Shock Compressed Matter for Use as a Dense Matter Diagnostic," Ph.D. Thesis University of California, Berkeley (2009).
- [33] http://www.us.schott.com/advanced_optics/english/products/index.html
- [34] <http://incomusa.com/products-process/faceplates/materials/>
- [35] <http://www.specinst.com/Products.html>